# Effect of Spatial and Temporal Resolution on the Accuracy of Motion Tracking Using 2D and 3D Cine Cardiac Magnetic Resonance Imaging Data

Kateřina Škardová, Tarique Hussain, Martin Genet, Radomír Chabiniok

## To cite this version:

Kateřina Škardová, Tarique Hussain, Martin Genet, Radomír Chabiniok. Effect of Spatial and Temporal Resolution on the Accuracy of Motion Tracking Using 2D and 3D Cine Cardiac Magnetic Resonance Imaging Data. FIMH 2023 - The 12th International Conference on Functional Imaging and Modeling of the Heart, Jun 2023, Lyon, France. pp.235-244, 10.1007/978-3-031-35302-4_24 . hal-04360493

HAL Id: hal-04360493
https://inria.hal.science/hal-04360493

Submitted on 21 Dec 2023

**HAL** is a multi-disciplinary open access archive for the deposit and dissemination of scientific research documents, whether they are published or not. The documents may come from teaching and research institutions in France or abroad, or from public or private research centers.

L'archive ouverte pluridisciplinaire **HAL**, est destinée au dépôt et à la diffusion de documents scientifiques de niveau recherche, publiés ou non, émanant des établissements d'enseignement et de recherche français ou étrangers, des laboratoires publics ou privés.

Distributed under a Creative Commons Attribution 4.0 International License

# Effect of spatial and temporal resolution on the accuracy of motion tracking using 2D and 3D cine cardiac magnetic resonance imaging data

Kateřina Škardová[1][0000-0002-9870-3438], Tarique Hussain[2][0000-0003-4091-992X], Martin Genet[3,4][0000-0003-2204-201X], and Radomír Chabiniok[2⋆][0000-0002-7527-2751]

[1] Department of Mathematics, Faculty of Nuclear Sciences and Physical Engineering, Czech Technical University in Prague, Prague, Czech Republic

[2] Division of Pediatric Cardiology, Department of Pediatrics, UT Southwestern Medical Center, Dallas, TX, USA

[3] Solid Mechanics Laboratory (LMS), École Polytechnique / Institut Polytechnique de Paris / CNRS, Palaiseau, France

[4] Inria, Palaiseau, France

**Abstract.** In this paper, we investigate the effect of spatial and temporal resolution of cardiac MRI cine images on the extracted left ventricle motion. A previously developed and validated finite-element-based image registration method was used for the motion extraction. The study is performed on three subjects, for which the standard 2D cine stack (SA) in short axis orientation and 3D cine MRI series were acquired. The set of acquired image series was augmented by artificially constructed SA-like cine series created from the 3D cine images. Image series with several combinations of spatial and temporal resolution were evaluated for each subject. The study showed a strong correlation between the slice thickness and the accuracy of extracted displacement in the longitudinal direction. The effect of a lower temporal resolution was shown to be less significant. This could prove useful to update current guidelines for cardiac MRI acquisitions.

**Keywords:** Cardiac magnetic resonance imaging · 3D cine MRI · left ventricular motion · image registration · equilibrated warping

## 1 Introduction

Cardiac magnetic resonance imaging (MRI) allows to assess the movement of the heart in vivo non-invasively. The analysis of motion patterns and derived quantities, such as the global measure of ejection fraction or local myocardial displacements or strains (typically in directions corresponding to the local coordinate system – radial, circumferential and longitudinal), is invaluable in the

---

[⋆] Corresponding author: `radomir.chabiniok@utsouthwestern.edu`

evaluation of the function of the ventricle. The quality of the image data – resolution, signal-to-noise ratio, etc. – may affect the accuracy of the quantities extracted from the image series, however.

In this paper, we intend to evaluate the difference in the tracked left ventricle (LV) motion that occurs when either a stack of 2D cine images with a through-plane resolution lower than the in-plane resolution is used (currently, standard clinical approach) or when a novel 3D cine image sequence providing isotropic spatial resolution is employed. We use a previously developed motion extraction method [4], already validated against open-access databases [9,5] as well as in silico data [1], and applied to multiple clinical projects (e.g., [2]). The study is performed on three subjects, for which the standard 2D cine stack in short axis orientation (SA cine) and in addition a new 3D cine MRI series ([6]) were acquired. In order to get a better insight into the relationship between the image resolution and the accuracy of the extracted quantities, additional SA-like cine series were constructed from the 3D cine images with various slice thicknesses (both thinner and thicker than the originally acquired 2D SA cine stack) and temporal resolutions.

## 2 Methods

### 2.1 Image acquisition

The computational study uses 3D and SA cine data from three asymptomatic patients with known repaired congenital heart disease and normal volumetric analysis. The data collections were performed under the ethical approval of Institutional Review Board of the UT Southwestern Medical Center, Dallas (STU 032016-009). The IRBs waived the need for a consent to use the anonymized retrospective data. The parameters of both types of cine images are shown in Table 1. The scan time of free-breathing 3D cine sequence was 5.9 ± 2.7 minutes [6] which is comparable to the acquisition time of the SA cine series using parallel imaging acceleration factor 2.

### 2.2 Construction of SA-like cine images

The 3D cine images were used to generate SA-like images by resampling a subdomain of the 3D cine image. The cine SA images of slice thickness $l$ mm constructed from the 3D cine will be denoted by $cSA_l$. These images were constructed with the same position and orientation in the real space, as were acquired the SA images.

First, the 3D cine image was resampled to the voxel size $1 \times 1 \times 1$ mm$^3$ using 3rd-order spline interpolation (using Python library SciPy). In the construction process, a voxel grid in the orientation of the acquired SA cine image and voxel spacing $1 \times 1 \times 1$ mm$^3$ was generated. Subsequently, the image intensities of the 3D cine image were projected onto this grid. The resolution of the constructed SA cine image was then decreased along the long axis to obtain the target spacing

| | Subject A | Subject B | Subject C |
|---|---|---|---|
| SA cine image series | | | |
| Time frames | 30 | 30 | 30 |
| Field of view [mm] | 280 × 280 × 88 | 300 × 300 × 90 | 330 × 330 × 110 |
| Spacing between slices [mm] | 8 | 10 | 10 |
| Original pixel dimensions [mm] | 1.79 × 1.93 | 1.8 × 2.38 | 1.79 × 2.15 |
| Resampled pixel dimensions [mm] | 1.09 × 1.09 | 0.93 × 0.93 | 1.03 × 1.03 |
| 3D cine image series | | | |
| Time frames | 30 | 30 | 30 |
| Field of view [mm] | 512 × 512 × 102 | 512 × 512 × 150 | 512 × 512 × 150 |
| Spacing between slices [mm] | 1.19 | 1.19 | 1.19 |
| Original pixel dimensions [mm] | 2 × 2.39 | 2 × 2.39 | 2 × 2.39 |
| Resampled pixel dimensions [mm] | 1.18 × 1.18 | 1.18 × 1.18 | 1.18 × 1.18 |

Table 1: Parameters of the SA and 3D cine image series.

by averaging the signals from the voxels within the given reconstructed 2D slice (i.e., a slice of thickness $n$ mm was obtained by averaging the image values in $n$ 1-mm slices). The slice thicknesses used in the constructed SA cine for each subject are shown in Table 2.

| | Slice thickness [mm] | | | | | |
|---|---|---|---|---|---|---|
| Subject A | 4 | **8** | 10 | 12 | | |
| Subject B | 5 | 8 | **10** | 12 | 15 | 18 |
| Subject C | 5 | 8 | **10** | 12 | 15 | 18 |

Table 2: Slice thickness of the constructed SA cine. The original slice thickness of the acquired SA cine is in bold.

### 2.3 Image series with lower temporal resolution

The original 30-time-frame image series were used to generate series with 1/2 and 1/3 temporal resolution, using the scheme shown in Figure 1. In the series with the original temporal resolution, $i$-th image is assumed to be acquired over the time interval $(t_i - \Delta t, t_i + \Delta t)$. The length of the acquisition time interval increases to $4\Delta t$ in the case of series with 1/2 temporal resolution, and to $6\Delta t$ in the case of series with 1/3 temporal resolution. The images in the series with the lower temporal resolution are generated by averaging the corresponding images from the original series while assuming the periodicity of the original data. The image series with 1/2 and 1/3 temporal resolution are generated for the 3D cine and two constructed SA cine series for all three subjects.

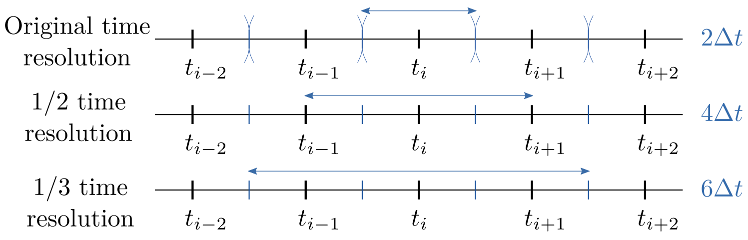

Fig. 1: The scheme of temporal averaging.

### 2.4 Segmentation of the left ventricle

The left ventricle (LV) is manually segmented from the first frame of the 3D cine corresponding to the end-diastole using the image processing framework MeVisLab[5]. The segmented surface meshes of the LV, exported from MeVisLab, are further remeshed in the finite element mesh generator GMSH[6] and subsequently used to generate volume meshes following the method described in [3]. In order to improve the tracking of boundary points of the LV, a layer of elements is added to the surface of the mesh using GMSH (see [4] for details). These elements are then removed before analyzing the deformation fields. The same mesh is used for all variants of cine images of each subject.

### 2.5 Finite element-based image registration with mechanical regularization

All image series are resampled to uniform resolution $1 \times 1 \times 1$ mm$^3$ by the spline interpolation before the motion tracking to ensure the correct integration of image similarity terms discussed below for all image series. The motion is extracted from the image series using a finite element-based image registration method, described in detail in [4]. In image registration, we generally want to determine the transformation between two images $I_0$ and $I_i$ of the object $\mathcal{B}$ – in our case the LV – acquired at times $t_0$ and $t_i$. The images are represented by image functions $I_0 : \Omega \to \mathbb{R}$ and $I : \Omega \to \mathbb{R}$, where $\Omega$ is the domain of the image. This problem of finding the transformation between the two images is ill-posed, and therefore we use a variational formulation suitable for the inclusion of regularization terms. The transformation, represented by mapping $\phi_i$ is then found as a minimizer of the following functional:

$$E(\phi_i) = E_{\text{image}}(\phi_i) + E_{\text{reg}}(\phi_i), \tag{1}$$

which combines the image similarity term $E_{\text{image}}(\phi_i)$ and the regularization term $E_{\text{reg}}(\phi_i)$. The image term evaluates the difference of image intensities of image

---

[5] https://www.mevislab.de

[6] https://gmsh.info

$I_0$ and $I_i$ at corresponding points:

$$E_{\mathrm{image}}(\phi_i) = \frac{1}{2} \int_{\Omega_0} \Big( I_i(\phi_i(\vec{X})) - I_0(\vec{X}) \Big)^2 \, \mathrm{d}\vec{X}, \tag{2}$$

where $\Omega_0 \subset \Omega$ is the domain occupied by the tracked object at the $t_0$. Alternatively, the transformation can be represented by displacement field $U_i$ such that $\phi_i(\vec{X}) = \vec{X} + U_i(\vec{X})$.

The selection of the regularization term may have a large impact on the extracted displacement. When imposing too strong assumptions, such as incompressibility of the tracked object or smoothness of mapping $\phi_i$, the actual motion captured in the image series can be suppressed. In this work, we use a regularization term proposed in [4], that penalizes deviation from the solution of a hyperelastic body in equilibrium with arbitrary boundary loads.

The mappings $\phi_i$ are determined as a solution of (1), for each frame $i$ of the series. Problem (1) is solved using the Newton method with gradient-free golden section line search. In the first frame ($i = 0$), the mapping $\phi_0 = \mathbb{I}$ is prescribed. The estimation of each subsequent $\phi_i$, $i > 0$ is initialized by the previously computed mapping $\phi_{i-1}$. The numerical solution is described in detail in [4], with the implementation of the solver freely available[7].

## 3 Results

In this section, we compare displacement fields extracted from different image series. In order to evaluate the difference between displacement fields $U^{\mathrm{ref}}$ and $U$, the following functions will be used:

- mean signed error in the radial direction (defined analogically for circumferential and longitudinal direction)

$$\mathrm{MSE_r}(t) = \frac{1}{|\Omega_0|} \int_{\Omega_0} \Big( U_r^{\mathrm{ref}}(\vec{X}, t) - U_r(\vec{X}, t) \Big) \, \mathrm{d}\vec{X} \tag{3}$$

- root-mean-square error in the radial direction (defined analogically for circumferential and longitudinal direction)

$$\mathrm{RMSE_r} = \sqrt{\frac{1}{T} \int_0^T \frac{1}{|\Omega_0|} \int_{\Omega_0} |U^{\mathrm{ref}_r}(\vec{X}, t) - U_r(\vec{X}, t)|^2 \mathrm{d}\vec{X} \mathrm{d}t} \tag{4}$$

- normalized root-mean-square error

$$\mathrm{NRMSE} = \frac{\sqrt{\frac{1}{T} \int_0^T \frac{1}{|\Omega_0|} \int_{\Omega_0} \|U^{\mathrm{ref}}(\vec{X}, t) - U(\vec{X}, t)\|^2 \mathrm{d}\vec{X} \mathrm{d}t}}{\sqrt{\frac{1}{T} \int_0^T \frac{1}{|\Omega_0|} \int_{\Omega_0} \|U^{\mathrm{ref}}(\vec{X}, t)\|^2 \mathrm{d}\vec{X} \mathrm{d}t}} \tag{5}$$

---

[7] https://gitlab.inria.fr/mgenet/dolfin_warp

### 3.1 The effect of slice thickness

In this section, we compare the accuracy of the extracted displacements obtained from image series with different slice thicknesses. Due to the absence of a ground truth, the displacement field extracted from the 3D cine image series will be used as reference value $U^{\mathrm{ref}}$.

The dependence of $\mathrm{RMSE_r}$, $\mathrm{RMSE_c}$ and $\mathrm{RMSE_l}$ on the slice thickness for all three subjects is shown in Figure 2. The figure shows the trend of an increasing error with an increasing slice thickness. $\mathrm{RMSE_l}$ is larger and increases steeper than both $\mathrm{RMSE_r}$ and $\mathrm{RMSE_c}$ for the same values of slice thickness in all three subjects.

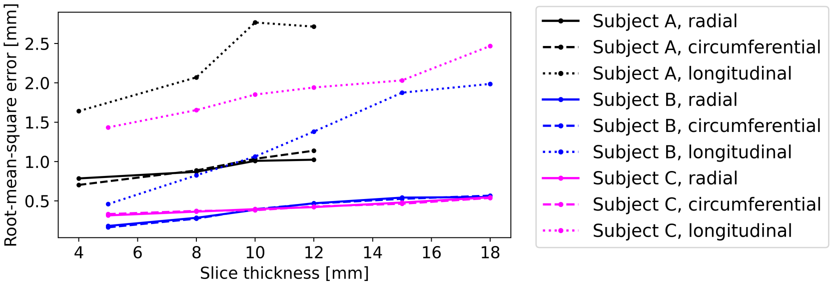

Fig. 2: The effect of the slice thickness on root-mean-square errors $\mathrm{RMSE_r}$, $\mathrm{RMSE_c}$ and $\mathrm{RMSE_l}$.

Table 3 shows the values of NRMSE for the cSA cine image series as well as the original SA image series $tSA_8$ and $tSA_{10}$. The error in displacement obtained from the original SA cine is larger than in the constructed image with the same slice.

| | $cSA_4$ | $cSA_8$ | $SA_8$ | $cSA_{10}$ | $cSA_{12}$ | | |
|---|---|---|---|---|---|---|---|
| Subject A | 45.07 | 55.77 | 55.31 | 72.11 | 71.98 | | |
| | $cSA_5$ | $cSA_8$ | $cSA_{10}$ | $SA_{10}$ | $cSA_{12}$ | $cSA_{15}$ | $cSA_{18}$ |
| Subject B | 13.22 | 23.21 | 30.41 | 45.86 | 38.82 | 51.23 | 54.18 |
| Subject C | 32.60 | 37.54 | 41.80 | 46.35 | 43.98 | 46.28 | 55.94 |

Table 3: Normalized root-mean-square errors NRMSE [%] evaluated for the cSA and SA cine image series.

In the scale of Figure 2, the values of RMSE in the radial and circumferential directions for Subject B and C appear to be almost identical. However, the temporal distributions of the errors differ, as can be seen in the plots of MSE for Subject C in Figure 3. The radial displacement is overestimated only in the systole, while the circumferential displacement is alternately underestimated and overestimated throughout the cardiac cycle. In the longitudinal direction, the sign of the mean error is also changing.

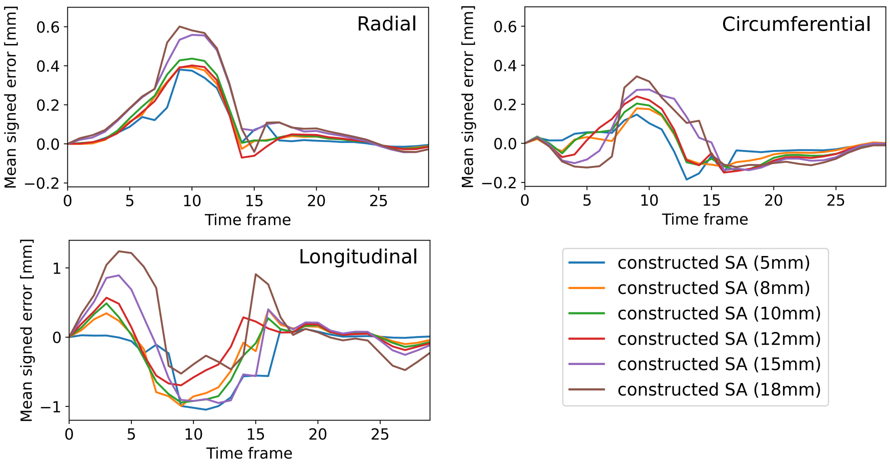

Fig. 3: Mean signed errors $\mathrm{MSE_r}$, $\mathrm{MSE_c}$ and $\mathrm{MSE_l}$ extracted from cine series with different spatial resolutions for subject C.

### 3.2 The effect of temporal resolution

In this section, we compare the accuracy of the displacement extracted from image series with the lower temporal resolution to the displacement field $U^{3D}$. We remark that the time interval $T$ in the definition of NRMSE (5) is independent of the temporal resolution. The time integrals are evaluated using the trapezoidal rule with $\Delta t = 1$, $\Delta t = 2$, and $\Delta t = 3$ for the original, 1/2, and 1/3 temporal resolution, respectively.

The values of NMRSE in Table 4 show that in the case of 3D cine, a decrease in temporal resolution leads to an increase in displacement error. This does not hold for the cSA images with a lower spatial resolution, where the accuracy of the extracted displacement field does not increase. In most cases, the change in NMRSE caused by the reduction in spatial resolution at fixed temporal resolution is larger than the change caused by the reduction in temporal resolution at fixed spatial resolution. The plots of MSE for Subject C are shown in Figure 4.

| Subject A | 3D (1.2 mm) | $cSA_8$ | $cSA_{12}$ |
|---|---|---|---|
| original resolution | 0 | 55.76 | 71.98 |
| 1/2 resolution | 10.97 | 51.89 | 70.30 |
| 1/3 resolution | 12.96 | 50.88 | 67.77 |
| **Subject B** | **3D (1.2 mm)** | **$cSA_{10}$** | **$cSA_{15}$** |
| original resolution | 0 | 30.40 | 51.23 |
| 1/2 resolution | 9.92 | 29.38 | 49.81 |
| 1/3 resolution | 12.27 | 29.34 | 49.70 |
| **Subject C** | **3D (1.2 mm)** | **$cSA_{10}$** | **$cSA_{15}$** |
| original resolution | 0 | 41.79 | 46.27 |
| 1/2 resolution | 10.97 | 38.63 | 42.52 |
| 1/3 resolution | 13.68 | 39.13 | 42.83 |

Table 4: Normalized root-mean-square errors NRMSE [%] evaluated for different temporal resolutions in the original 3D cine (voxel size 1.2 mm) and constructed SA cine of selected slice thicknesses 8-15 mm.

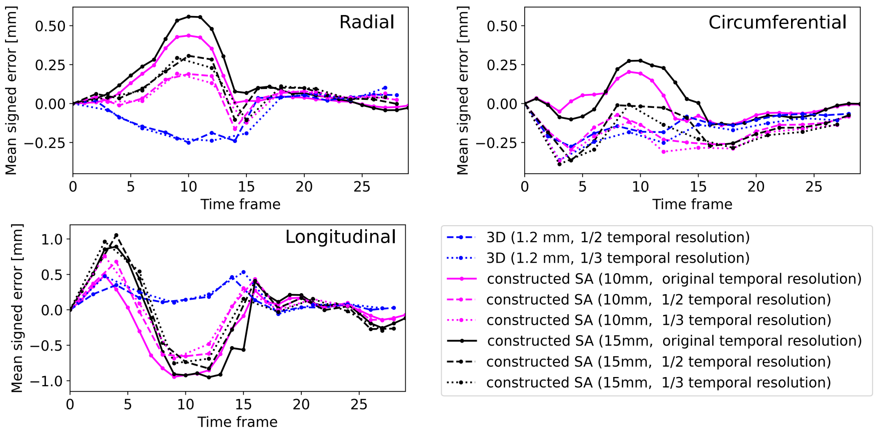

Fig. 4: Mean signed errors $\mathrm{MSE_r}$, $\mathrm{MSE_c}$ and $\mathrm{MSE_l}$ extracted from cine series with different spatial and temporal resolutions for subject C.

## 4 Discussion & Conclusion

We investigated the dependence between spatial and temporal resolution of MR cine images and the accuracy of LV motion extracted from the images. A previously developed and validated motion tracking method was used. The study was performed using an acquired series of 3D and SA cine images and SA-like constructed cine image series, which allowed to extend the set of combinations of spatial and temporal resolution.

Given the limitation of working directly with image data, the required spatial and temporal resolution in the constructed image series was obtained by appropriately averaging the original images. The averaging of sub-slices was done to simulate the 2D acquisition with an optimal ramp-like slice selection gradient. The temporal averaging was designed as an image-space approximation of the segmented filling of k-space for each time frame.

The displacements extracted from the image series with various spatial and temporal resolutions were compared with the displacement obtained from the 3D cine with the original temporal resolution. For all subjects, the displacement error was largest in the longitudinal direction. Moreover, the error in the longitudinal direction was also affected by the increase in slice thickness. The effect of a reduced temporal resolution on the studied quantities proved to be smaller than the effect of slice thickness. The effect on other features of the LV motion, such as the strain or strain rate should be investigated in the future.

The trend in the dependency of displacement accuracy on the spatial and temporal resolution was consistent in all three subjects. However, the RMSE, as well as the NRMSE, were higher for Subject A than for Subjects B and C. This is possibly due to a lower ratio between the dimensions of the ventricle and the voxel size, which may result in more voxels being influenced by the partial volume effect.

The present study provides a good insight into the use of 3D cine in routine clinical acquisitions. We have shown that no information is lost compared to standard multiple 2D cine acquisition and a higher quality local motion pattern can possibly be extracted. A similar approach using constructed images can also be used to quantify expected acquisition errors with high undersampling (in space or time), e.g., in clinical applications requiring real-time acquisition to capture complex physiology [7,8].

## Acknowledgements

This work was supported by MEYS of the Czech Republic under the OP RDE grants no. CZ2.11/0/0/16_019/0000765, by Ministry of Health of the Czech Republic project no. NV19-08-00071. This work was also supported by the Inria-UTSW Associated Team TOFMOD.

## References

1. Berberoğlu, E., Stoeck, C.T., Moireau, P., Kozerke, S., Genet, M.: In-silico study of accuracy and precision of left-ventricular strain quantification from 3D tagged MRI. PLOS ONE **16**(11) (2021). https://doi.org/10.1371/journal.pone.0258965, https://dx.plos.org/10.1371/journal.pone.0258965
2. Castellanos, D.A., Škardová, K., Bhattaru, A., Greil, G., Tandon, A., Dillenbeck, J., Burkhardt, B., Hussain, T., Genet, M., Chabiniok, R.: Left ventricular torsion obtained using equilibrated warping in patients with repaired tetralogy of Fallot. Pediatric Cardiology **42**(6), 1275–1283 (2021). https://doi.org/10.1007/s00246-021-02608-y

3. Genet, M., Lee, L.C., Nguyen, R., Haraldsson, H., Acevedo-Bolton, G., Zhang, Z., Ge, L., Ordovas, K., Kozerke, S., Guccione, J.M.: Distribution of normal human left ventricular myofiber stress at end diastole and end systole: a target for in silico design of heart failure treatments. Journal of Applied Physiology **117**, 142–152 (2014). https://doi.org/10.1152/japplphysiol.00255.2014, http://www.ncbi.nlm.nih.gov/pubmed/24876359
4. Genet, M., Stoeck, C.T., Von Deuster, C., Lee, L.C., Kozerke, S.: Equilibrated warping: Finite element image registration with finite strain equilibrium gap regularization. Medical image analysis **50**, 1–22 (2018)
5. Lee, L.C., Genet, M.: Validation of Equilibrated Warping—Image Registration with Mechanical Regularization—On 3D Ultrasound Images. In: Functional Imaging and Modeling of the Heart: 10th International Conference, FIMH 2019, Bordeaux, France, June 6–8, 2019, Proceedings 10. pp. 334–341. Springer, Bordeaux, France (2019). https://doi.org/10.1007/978-3-030-21949-9_36
6. Moghari, M.H., Barthur, A., Amaral, M.E., Geva, T., Powell, A.J.: Free-breathing whole-heart 3D cine magnetic resonance imaging with prospective respiratory motion compensation. Magnetic resonance in medicine **80**(1), 181–189 (2018)
7. Ruijsink, B., Velasco Forte, M.N., Duong, P., Asner, L., Pushparajah, K., Frigiola, A., Nordsletten, D., Razavi, R.: Synergy in the heart: RV systolic function plays a key role in optimizing LV performance during exercise. American Journal of Physiology-Heart and Circulatory Physiology **319**(3), H642–H650 (2020)
8. Ruijsink, B., Zugaj, K., Wong, J., Pushparajah, K., Hussain, T., Moireau, P., Razavi, R., Chapelle, D., Chabiniok, R.: Dobutamine stress testing in patients with Fontan circulation augmented by biomechanical modeling. PLoS one **15**(2), e0229015 (2020)
9. Tobon-Gomez, C., De Craene, M., Mcleod, K., Tautz, L., Shi, W., Hennemuth, A., Prakosa, A., Wang, H., Carr-White, G., Kapetanakis, S., et al.: Benchmarking framework for myocardial tracking and deformation algorithms: An open access database. Medical image analysis **17**(6), 632–648 (2013)